

Electronic structure study of the charge-density-waveKondo lattice $CeTe_3$

Bo Wang(王博), Rui Zhou(周锐), Xuebing Luo(罗学兵), Yun Zhang(张云), and Qiuyun Chen(陈秋云)
Citation: Chin. Phys. B, 2023, 32 (**9**): 097103. DOI: 10.1088/1674-1056/acb41e
Journal homepage: http://cpb.iphy.ac.cn; http://iopscience.iop.org/cpb

What follows is a list of articles you may be interested in

Single crystal growth and electronic structure of Rh-doped $Sr_3Ir_2O_7$

Bingqian Wang(王冰倩), Shuting Peng(彭舒婷), Zhipeng Ou(欧志鹏), Yuchen Wang(王宇晨), Muhammad Waqas, Yang Luo(罗洋), Zhiyuan Wei(魏志远), Linwei Huai(淮琳崴), Jianchang Shen(沈建昌), Yu Miao(缪宇), Xiupeng Sun(孙秀鹏), Yuewei Yin(殷月伟), and Junfeng He(何俊峰)
Chin. Phys. B, 2023, 32 (**8**): 087108. DOI: 10.1088/1674-1056/acd7d5

Electronic structure of cuprate-nickelate infinite-layer heterostructure

Dachuan Chen(陈大川), Paul Worm, Liang Si(司良), Chunxiao Zhang(张春小), Fenglin Deng(邓凤麟), Peiheng Jiang(蒋沛恒), and Zhicheng Zhong(钟志诚)
Chin. Phys. B, 2023, 32 (**8**): 087105. DOI: 10.1088/1674-1056/acd368

Electronic states of domain walls in commensurate charge density wave ground state and mosaic phase in 1*T*-TaS_2

Yan Li(李彦), Yao Xiao(肖遥), Qi Zheng(郑琦), Xiao Lin(林晓), Li Huang(黄立), and Hong-Jun Gao(高鸿钧)
Chin. Phys. B, 2023, 32 (**7**): 077101. DOI: 10.1088/1674-1056/accd4f

Flat band in hole-doped transition metal dichalcogenide observed by angle-resolved photoemission spectroscopy

Zilu Wang(王子禄), Haoyu Dong(董皓宇), Weichang Zhou(周伟昌), Zhihai Cheng(程志海), and Shancai Wang(王善才)
Chin. Phys. B, 2023, 32 (**6**): 067103. DOI: 10.1088/1674-1056/acc7f9

Tri-hexagonal charge order in kagome metal CsV_3Sb_5 revealed by ^{121}Sb nuclear quadrupole resonance

Chao Mu(牟超), Qiangwei Yin(殷蔷薇), Zhijun Tu(涂志俊), Chunsheng Gong(龚春生), Ping Zheng(郑萍), Hechang Lei(雷和畅), Zheng Li(李政), and Jianlin Luo(雒建林)
Chin. Phys. B, 2022, 31 (**1**): 017105. DOI: 10.1088/1674-1056/ac422c

---

Electronic structure study of the charge-density-wave Kondo lattice $CeTe_3$

Bo Wang(王博)[†], Rui Zhou(周锐)[†], Xuebing Luo(罗学兵), Yun Zhang(张云)[‡], and Qiuyun Chen(陈秋云)[§]

Science and Technology on Surface Physics and Chemistry Laboratory, Mianyang 621907, *China*

(Received 17 October 2022; revised manuscript received 25 December 2022; accepted manuscript online 18 January 2023)

The behaviors of f electrons are crucial for understanding the rich phase diagrams and ground-state properties of heavy fermion (HF) systems. The complicated interactions between f electrons and conduction electrons largely enrich the basic properties of HF compounds. Here the electronic structure, especially the f-electron character, of the charge-density-wave (CDW) Kondo lattice compound $CeTe_3$ has been studied by high-resolution angle-resolved photoemission spectroscopy. A weakly dispersive quasiparticle band near the Fermi level has been observed directly, indicating hybridization between f electrons and conduction electrons. Temperature-dependent measurements confirm the localized to itinerant transition of f electrons as the temperature decreases. Furthermore, an energy gap formed by one conduction band at low temperature is gradually closed with increasing temperature, which probably originates from the CDW transition at extremely high temperature. Additionally, orbital information of different electrons has also been acquired with different photon energies and polarizations, which indicates the anisotropy and diverse symmetries of the orbitals. Our results may help understand the complicated f-electron behaviors when considering its interaction with other electrons/photons in $CeTe_3$ and other related compounds.

Keywords: 4f-electron, charge-density-wave, electronic structure, angle-resolved photoemission spectroscopy

PACS: 71.20.Eh, 71.27.+a, 79.60.–i, 71.45.Lr **DOI:** 10.1088/1674-1056/acb41e

1. Introduction

Investigating the physical connotation of f electrons in heavy fermion (HF) systems is a challenging subject. Consensus exists that the exotic quantum states such as unconventional superconductivity, magnetic order, hidden order and non-Fermi liquid behaviors are all closely related to f electrons in HF systems.[1–3] In HF materials, Kondo entanglement plays a crucial role which is basically manifested by a logarithmic increase of electric resistivity and a following decrease of the resistivity as the heavy quasiparticle emerges with decreasing temperature. The hybridization between f electrons and conduction electrons (f–c hybridization) generates the composite quasiparticles with heavy effective mass and a larger Fermi surface (FS) volume.[4,5] In fact, the f electrons exhibit dual properties, i.e., both localized and itinerant traits.[6,7] They are localized at high temperature and become itinerant as the temperature decreases by hybridizing with conduction electrons.[8,9] Understanding the features of f electrons is significant to explore the origin of the physical properties of HF systems. In this regard, a fundamental and indispensable part is direct observation of the electronic structure, especially the f-electron character, of HF systems.

Many rare earth tellurides RTe_n ($n = 2, 3$) display extraordinary properties, such as charge-density-wave (CDW) transition and pressure-induced superconductivity.[10–13] However, $CeTe_n$ ($n = 2, 3$) compounds do not turn into the superconductivity state with applied pressure. At ambient pressure, an antiferromagnetic transition temperature is found as low as 4.3 K for $CeTe_2$, while $CeTe_3$ is antiferromagnetic below $T_N = 2.8$ K.[14] Besides, $CeTe_3$ shows a CDW state at room temperature, however, the transition temperature has never been observed even when the temperature is raised up as high as 500 K.[15,16]

Measurements of transport properties found a weak Kondo lattice behavior below approximately 10 K before $CeTe_3$ orders into an antiferromagnetic ground state at $T_N = 2.8$ K. This implies the existence of Kondo entanglement in $CeTe_3$ at low temperature.[17] Study of $CeTe_3$ using nuclear magnetic resonance (NMR) leads to the conclusion that there is coupling between the Te (1) conduction electron band and the Ce local moment, which induces the temperature dependence of the ^{125}Te (1) NMR spectrum. $CeTe_3$ also has an unconventional CDW interacting between the Ce local moments and the strong Ce spin fluctuations.[18,19] Scanning tunneling spectroscopy (STS) and Raman scattering measurements reveal that the CDW transition opens an energy gap of about 240 meV–740 meV in optimally nested regions on the FS.[20,21] Previous angle-resolved photoemission spectroscopy (ARPES) studies reported multiple shadow bands and FS reconstruction induced by the CDW transition.[10,22] Time-resolved angle-resolved photoemission spectroscopy (tr-ARPES) study reported the collective response of $CeTe_3$ in the

[†]These authors contributed equally to this work.
[‡]Corresponding author. E-mail: thu_zhangyun@126.com
[§]Corresponding author. E-mail: sheqiuyun@126.com

© 2023 Chinese Physical Society and IOP Publishing Ltd

CDW phase. Momentum-dependent analysis combined with density-functional theory (DFT) frozen phonon calculations reveals different coupling to the band structure for amplitude modes and optical phonons.[23] However, details of the electronic structure, especially how the f electrons interact with the conduction electrons in the CDW state, are still unexplored. Furthermore, the difference in f-electron features in the CDW state and the normal state in other heavy fermion materials also deserves special attention.

In this paper, we explore the electronic structure of $CeTe_3$ at different temperatures by ARPES and observe the localized to itinerant transition of f electrons and the opening of an energy gap in one conduction band which is probably related to the CDW state. We also present the electronic structure of $CeTe_3$ with different photon energies and polarizations. Measurements with differently polarized light are conducted to distinguish information from different electron orbitals. Meanwhile, with 7 eV and 21.2 eV photons, the fine structure of the bulk and surface states are obtained.

2. Experimental details

High-quality single crystals of $CeTe_3$ were grown by the flux method with a mixture of alkali chlorides as the flux.[24] Single-crystal x-ray diffraction (XRD) data, shown in Fig. 1(a), were acquired on a PANalytical X' Pert Pro diffractometer (Cu K_α radiation). As presented in Figs. 1(b)–1(d), electrical resistivity and magnetization data were collected by a Quantum Design physical properties measurement system (PPMS). Electrical resistivity was measured based on the four-point electrodes method with its ACT module and magnetization measurement was made by a SQUID magnetometer. All ARPES data displayed here except those shown in Fig. 6 were obtained at the "Dreamline" beamline of the Shanghai Synchrotron Radiation Facility (SSRF) with a Scienta DA30 analyzer. The energy resolution is 17 meV and angle resolution is 0.2°. The samples were cleaved along the b axis in ultra-high vacuum conditions at 18 K before performing ARPES measurements. The base pressure of the system was below 2×10^{-10} mbar during the whole measurement. Laser ARPES and He-lamp ARPES data were collected by the DA30L analyzer and the base pressure was below 8×10^{-11} mbar. The energy and angle resolutions for laser ARPES are 2.5 meV and 0.2°, respectively. The energy and angle resolutions for He-lamp ARPES are better than 20 meV and 0.2°, respectively.

3. Results and discussion

The XRD result shown in Fig. 1(a) indicates the cleavage plane of the as-grown single crystal is the (010) plane of $CeTe_3$. Meanwhile, the absence of other miscellaneous peaks shows that the quality of $CeTe_3$ is fairly good. As shown in Fig. 1(b), the electrical resistivity versus temperature curve displays a rather obvious linear behavior from 20 K to 300 K with current flowing in the ac-plane. In the range of 3 K to 10 K, there is a plateau where the resistivity nearly remains invariant with decreasing temperature. It is similar to the logarithmic increase with decreasing temperature and may indicate a weak Kondo interaction.[17] Around 3 K, a distinct kink appears which is an indication of the magnetic transition.[25] The residual resistivity ratio (RRR) of these samples reaches 71, implying their good crystal qualities. Figure 1(c) shows the temperature dependence of the susceptibility χ and inverse susceptibility $1/\chi$ with the magnetic field $H = 0.5$ T perpendicular to the b axis ($H\perp b$). Above 50 K, $1/\chi$ displays a nearly linear dependence, which is in good agreement with the Curie–Weiss law, and indicates the Ce ions behave in the typical localized model.[26] There is a broad hump below 50 K in the $1/\chi$–T curve. This obvious character may relate to the crystalline-field-effect.[14] Magnetization as a function of the field with the magnetic field perpendicular to the b axis ($H\perp b$) at different temperatures is shown in Fig. 1(d). At 30 K, a linear lineshape is observed. With decreasing temperature, there is an intermediate state between the linear lineshape and obvious magnetization saturation at 5 K. The saturation susceptibility at 2 K is smaller than that at 3 K. The smaller saturation susceptibility at 2 K is consistent with the trend of resistivity in Fig. 1(b) and reveals the possibility of an antiferromagnetic transition below 3 K.[14]

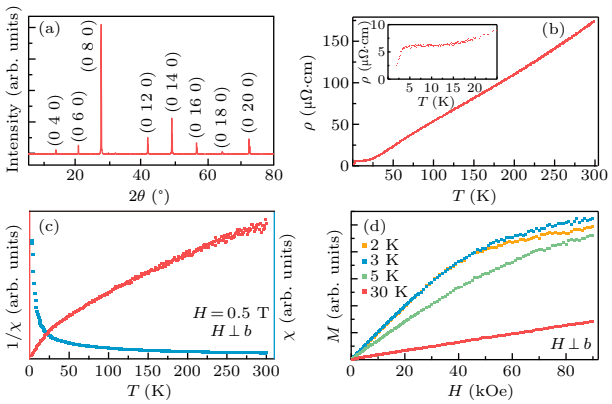


Fig. 1. Physical properties of $CeTe_3$. (a) Single-crystal XRD data of $CeTe_3$. (b) Electrical resistivity of $CeTe_3$ as a function of temperature for currents flowing in the ac-plane. The inset on the top left shows the zoomed-in diagram below 25 K. (c) Temperature dependence of susceptibility χ (blue dots) and inverse susceptibility $1/\chi$ (red dots) with a magnetic field of 0.5 T perpendicular to the b axis. (d) Magnetization as a function of the field with the magnetic field perpendicular to the b axis at 2 K, 3 K, 5 K, and 30 K.

The crystal structure of $CeTe_3$ is sketched in Fig. 2(a), which shows a layered ABBA stacking order along the b axis. Here, A stands for the flat Te–Te slabs and the zigzag Ce–Te slabs are described as B. The considerable b/a ratio of nearly six reflects its two-dimensional feature. As the gray shaded region between two Te–Te slabs shows, the weak interlayer force makes it easy to form a cleavage surface and the topmost

Te atoms are exposed. In such a flat square-net structure, the p_x and p_z orbitals of the Te atoms hybridize with each other and a square-net electron cloud naturally forms,[27] while the p_y orbital perpendicular to the Te–Te layers has a disposition to interact with the electrons of the layers beneath. As Figs. 2(b) and 2(c) show, when the bulk crystal structure is considered, the periodicity of Te–Te layers is smaller than the bulk periodicity, leading to the change of the two-dimensional first Brillouin zone (FBZ). We depict the two-dimensional FBZ in Fig. 2(d). The dashed black lines reflect the surface state of the topmost Te–Te slab and the solid red lines include the bulk information which is induced by a larger lattice constant mainly resulting from the Ce–Te slabs. The observed FS in Fig. 2(e) matches well with the projected BZ calculated with the lattice constants considering the topmost Te–Te slab, while it differs a little from the calculated BZ with the bulk lattice constants. Since $CeTe_3$ is a layered structure and easy to cleave, it is possible that the FS contribution is primarily from the Te–Te layer-terminated surface. Meanwhile, a slight contribution from the Ce–Te layers may also exist. The topology of the FS consists of three electron pockets, namely, a square-like electron pocket around the Γ point, the electron pocket between the Γ and M points and another electron pocket around the M point. In brief, it shows the typical square-net pocket feature and the FS nesting induces CDW formation in $CeTe_3$.[20,22] Detailed band dispersion derived from the photoemission intensity plots along the high-symmetry Γ–M and Γ–X directions are shown in Figs. 2(f)–2(g). Along Γ–M, three bands cross the Fermi level, which are marked with α, β and γ, respectively. Two bands marked with ε and η are below E_F. The electron-like γ band encloses the Γ point, forming a square-like electron pocket around the zone center. The pocket between the Γ and M points consists of electron-like α and β bands. As displayed in Fig. 2(g), β, γ, ε and η bands can also be clearly observed along Γ–X, which show similar features to those along the Γ–M direction.

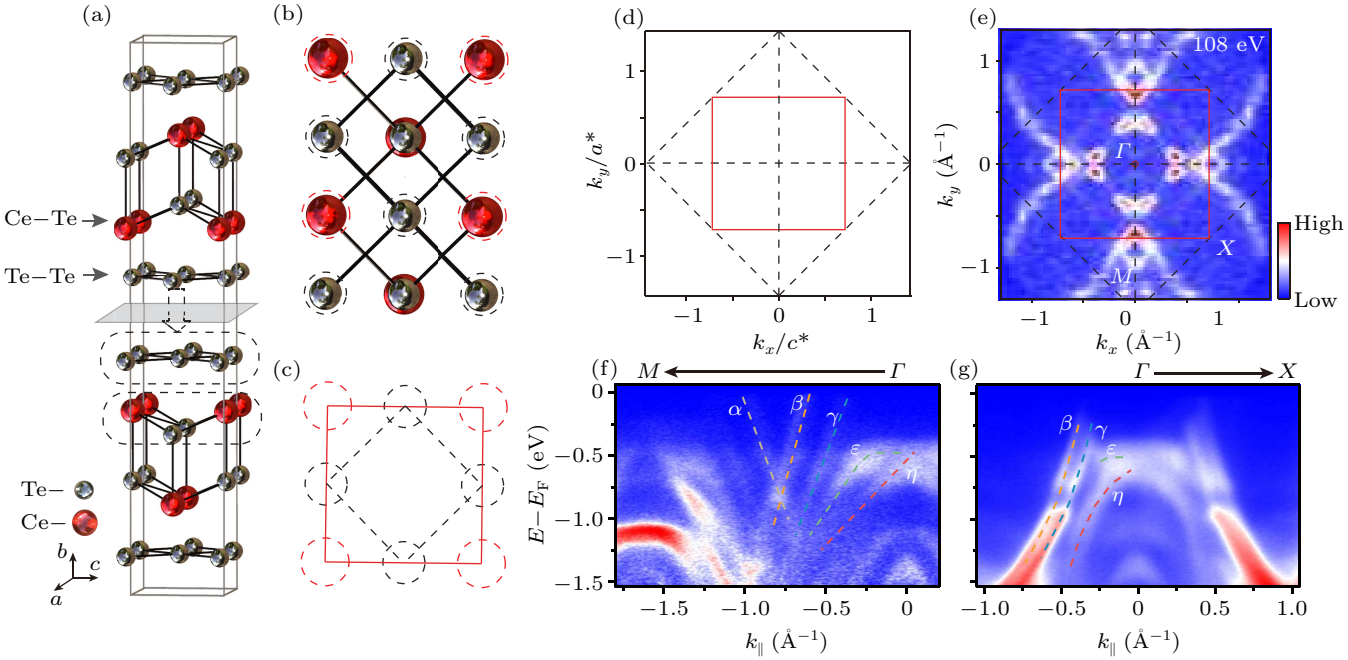


Fig. 2. Crystal structure and electronic structure of $CeTe_3$. (a) Crystal structure of $CeTe_3$. Ce and Te atoms are in red and gray, respectively. The shaded area indicates the cleavage plane. (b) Top view of $CeTe_3$ after cleaving. The dotted circles are also shown in panel (c). (c) Positions of Ce (red) and Te (gray) atoms in real space. (d) The Brillouin zone (BZ) of $CeTe_3$. The BZ of the bulk $CeTe_3$ is depicted by the solid red line and BZ of the topmost two-dimensional Te–Te slab is drawn in the dashed black line. (e) Photoemission intensity map of $CeTe_3$ at E_F with 108 eV photon energy. The intensity is integrated over a window of $[E_F - 10$ meV, $E_F + 10$ meV$]$. The setting of the BZ is the same as that in panel (d). (f)–(g) Photoemission intensity distributions along panel (f) Γ–M and panel (g) Γ–X at 18 K. Some typical bands are indicated with colored dashed lines.

To enhance the f-electron photoemission intensity, resonant ARPES measurements were performed at the Ce 4d–4f transition edge with 121 eV photons. Figures 3(a) and 3(b) show the comparison of the ARPES data with on-resonant 121 eV photons and with off-resonant 114 eV photons along Γ–M. In Fig. 3(a), strongly dispersive bands which are centered around the Γ and M points dominate the off-resonant spectra. Compared with off-resonant photoemission intensity distributions, the on-resonant spectrum reveals three nearly flat bands at binding energies of 0.14 eV, 0.54 eV and 2.95 eV. These flat bands reflect the enhancement of the Ce 4f emission with the on-resonant condition. This is similar to the 4f-electron features observed in other Ce-based materials such as $CeCoIn_5$, $CeRhIn_5$ and $CeIrIn_5$.[28–30] However, the energy positions of the three flat f bands are further away from the Fermi level compared with other Ce-based compounds; in particular, the position of the f band near the Fermi level is obviously below the Fermi level. The one at 2.95 eV below E_F

with strong intensity can be assigned to the initial $4f^0$ state, while those near 0.14 eV and at 0.54 eV below E_F are from the $4f^1_{5/2}$ state and its spin–orbital coupling (SOC) sideband $4f^1_{7/2}$ component, respectively.[28,31] The flat band at 2.95 eV below E_F derives from the pure charge excitation ($4f^1 \rightarrow 4f^0$) and is generally known as the ionization peak.[32] And the feature near 0.14 eV is actually the tail of the Kondo resonance above E_F. We further find the Kondo resonance state exhibits a dispersive characteristic (red dotted line) which can be observed near the M point, as shown in Fig. 3(d). Moreover, the intensity of the $4f^1_{5/2}$ state is much stronger than that of the $4f^1_{7/2}$ and $4f^0$ states. These features indicate the existence of the hybridization between Ce 4f state and the conduction bands.[33]

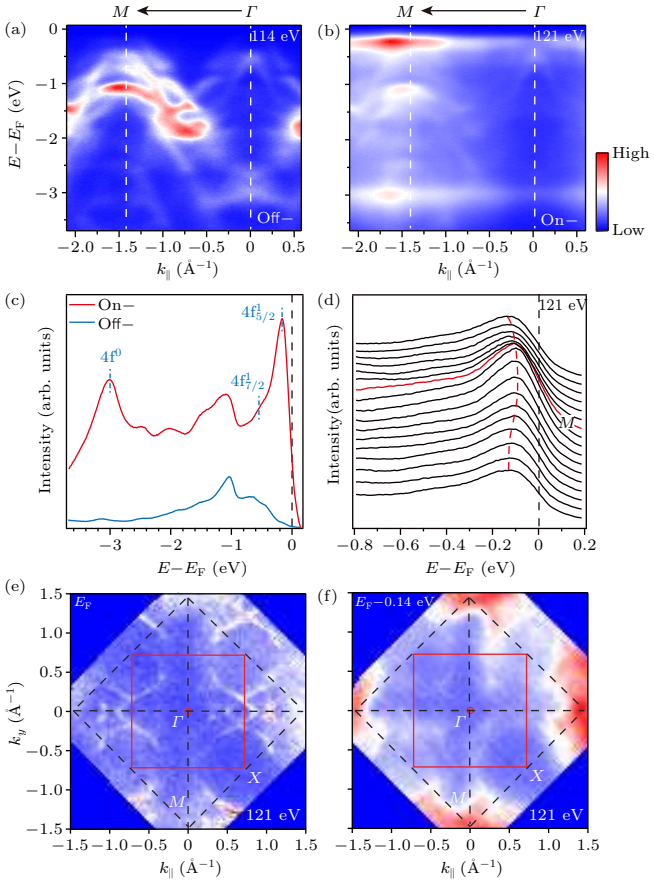


Fig. 3. Off/on-resonant ARPES results. (a)–(b) Photoemission intensity distributions of $CeTe_3$ along Γ–M taken at 20 K with (a) off-resonance (114 eV) and (b) on-resonance (121 eV). (c) Angle-integrated energy distribution curves (EDCs) of $CeTe_3$ with on- and off-resonance over the momentum range of [−2.1 Å^{-1}, −0.7 Å^{-1}]. The f band positions are marked with blue dashed lines. (d) EDCs of $CeTe_3$ with 121 eV photons near the Fermi level. The red solid curve marks the M point and the dashed red curve represents the f band dispersion near the M point. (e) Photoemission intensity map of $CeTe_3$ at E_F with 121 eV photons. The intensity is integrated over a window of [E_F-30 meV, E_F+30 meV]. (f) Isoenergetic surface of $CeTe_3$ at 0.14 eV below E_F with 121 eV photons. The intensity is integrated over a window of [E_F-30 meV, E_F+30 meV].

Meanwhile, the spectral intensity of the $4f^1_{5/2}$ state exhibits pronounced momentum dependence. The spectra of the f state centered at the M point (red solid curve) in Figs. 3(e) and 3(f) show strong intensity, while at other momentum locations, the intensity seems homogeneous and relatively weak. To comprehensively understand the contribution of f electrons to the Fermi surface, a photoemission intensity map at E_F with 121 eV is displayed in Fig. 3(e). In comparison with that in Fig. 2(e), more f-electron features are observed and the spectral intensity is relatively strong. Moreover, the constant energy surface at 0.14 eV below E_F, where the $4f^1_{5/2}$ state is located as shown in Fig. 3(f), reveals similar f-electron features but with much stronger spectral intensity.

Figure 4 shows the detailed temperature evolution of the resonant ARPES data along Γ–X from 25 K to 253 K. From Figs. 4(a1)–4(a5), the photoemission intensity is dominated by the strongly dispersive conduction bands. At 0.14 eV and 2.95 eV below E_F, two f-electron band features are obvious. As the red arrow indicates in Fig. 4(a1), an energy gap about 0.30 eV is observed in this conduction band. With increasing temperature, the energy gap seems to be closing slowly and detailed information of the gap will be discussed later. In order to clarify the evolution of f-electron with temperature, figure 4(b) displays the temperature dependence of the EDCs near E_F around the Γ point. As previously mentioned, the f-electron feature near E_F originates from the $4f^1_{5/2}$ state. With increasing temperature, no obvious shift of the peak position is observed, but the change of strength is obvious. The lower the temperature, the stronger the f-electron strength. This shows that with decreasing temperature, f electrons go through the localized to itinerant transition. However, because the peak position of the f states do not show obvious change as shown in Fig. 4(b), we propose the f states are not related to the CDW state transition in $CeTe_3$. This is consistent with the high CDW transition of $CeTe_3$. Consequently, the abnormal energy position of the $4f^1_{5/2}$ state originates from other reasons, which need further investigations. In addition, the temperature dependence of the energy gap observed in Figs. 4(a1)–4(a5) is also shown in Fig. 4(c). A conduction band opens an energy gap around the X point and the gap is located at about 0.50 eV–0.85 eV below E_F. As the EDCs show in Fig. 4(c), with increasing temperature, the strength of the gap decreases and the size of the gap becomes smaller. To explain the change of the energy gap size more clearly, we carried out multipeak fitting processing. In Fig. 4(d), it is clear that the size of the gap is mainly about 0.20 eV–0.32 eV and has a negative correlation with temperature. The above phenomenon shows that the gap is gradually closed with the increase of temperature. The behavior in this temperature range is similar to that of CuTe and VTe_2, which are also CDW materials, indicating that the existence of the gap may be related to the formation of the CDW state.[34,35] However, since the CDW transition temperature is extremely high and more than 500 K, we cannot observe the closing of the gap at this point.

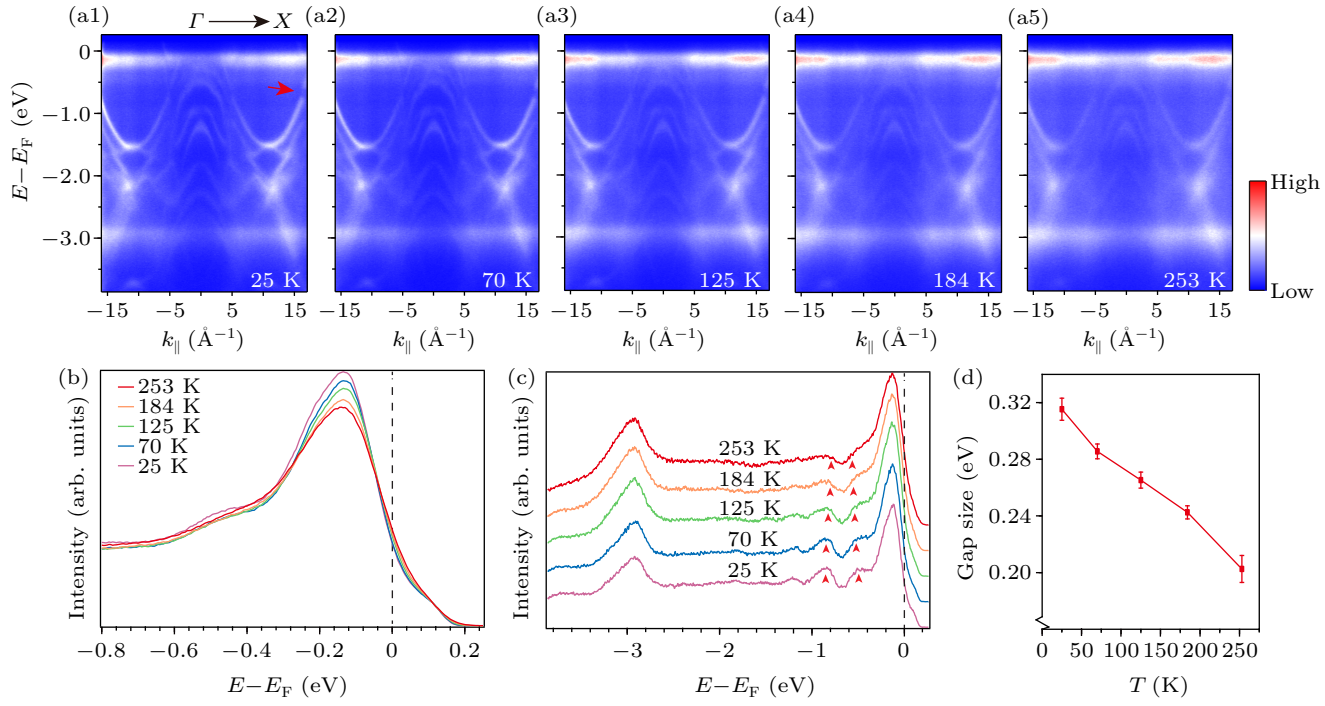


Fig. 4. Electronic structure of $CeTe_3$ as a function of temperature. (a1)–(a5) Resonant (121 eV) ARPES data of $CeTe_3$ taken along Γ–X with 121 eV at the labelled temperatures. (b) Temperature dependence of the EDCs around the Γ point in panel (a). (c) Temperature dependence of the EDCs around the position indicated by the red arrow in panel (a1). (d) Temperature dependence of the gap. The size of the gap is obtained by multipeak fitting using the Lorentz function. The error bar comes from the mean value and standard deviation obtained by fitting.

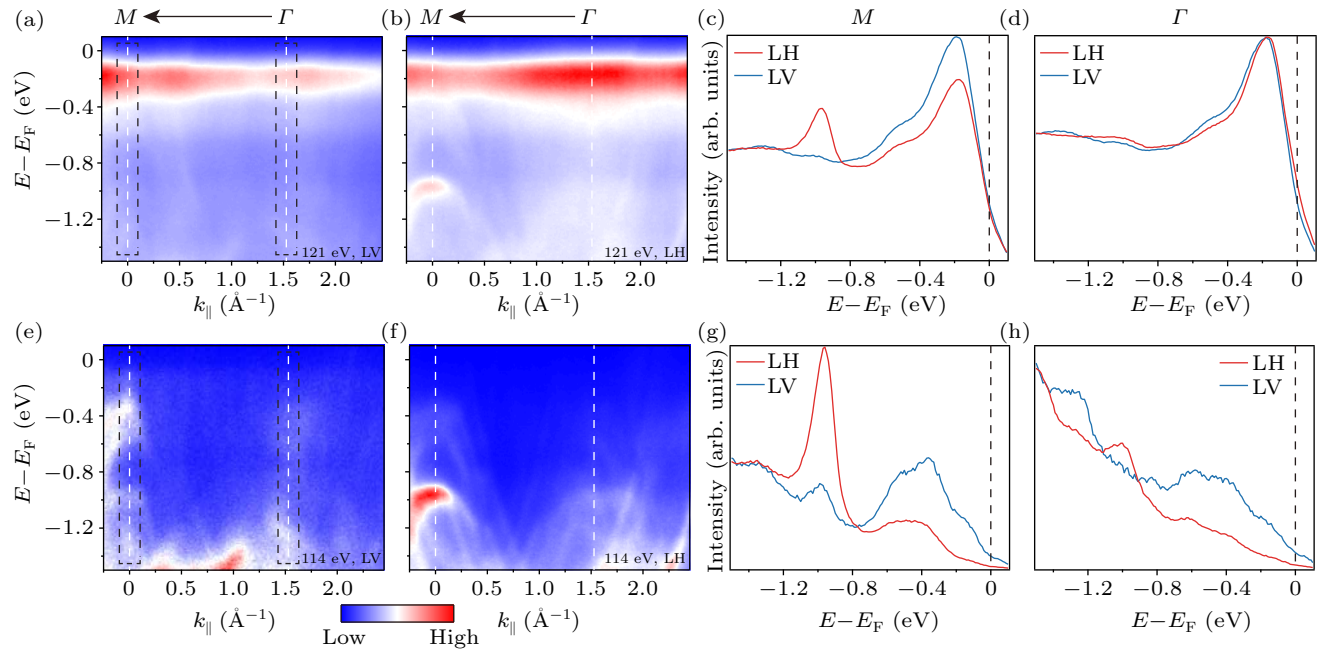


Fig. 5. LV- and LH-polarized ARPES results. (a), (b) Photoemission intensity distributions of $CeTe_3$ taken along Γ–M with 121 eV LV- and LH-polarized photons, respectively. (c), (d) Comparison of the angle-integrated EDCs of the black dashed regions in panel (a) with 121 eV LV- and LH-polarized photons, respectively. (e), (f) Photoemission intensity distributions of $CeTe_3$ taken along Γ–M with 114 eV LV- and LH-polarized photons, respectively. (g), (h) Comparison of the angle-integrated EDCs with 114 eV LV- and LH-polarized photons, respectively. The integrated window in panel (e) is marked with the black dashed lines.

To illustrate the effect of different polarized photons on the band structure, LV- and LH-polarized ARPES measurements were further conducted as shown in Fig. 5. From Figs. 5(a)–5(d), there are three prominent features: (a) the intensity of f bands near the Fermi level with LV-polarized photons is stronger than with LH polarization near the M point, but the change of intensity is not apparent near the Γ point. (b) A hole-like band near the M point with LH-polarized photons shows strong dispersion which is located at about 1 eV below E_F, while it is absent with LV-polarized light. (c) The $4f^1_{7/2}$ state near the M point is enhanced when the polarization is changed from LH to LV, while the state near the Γ

point does not show significant difference with the light. The anisotropy of the orbitals may be a pivotal factor that induces the above phenomena. The variations of the f band and the band at 1 eV below E_F (see more apparent in panels (e)–(h)) with different polarized photons display obvious discrepancy, which indicates diverse orbital symmetries.

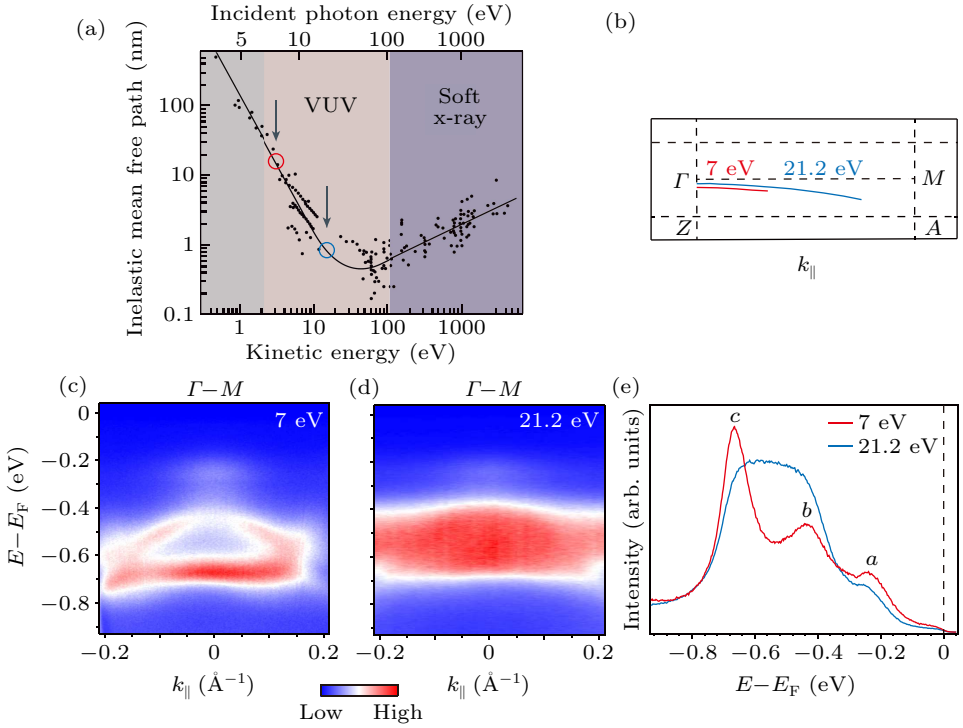


Fig. 6. Comparison of the electronic structures between surface and bulk of $CeTe_3$. (a) The inelastic mean free path of the photoelectrons as a function of kinetic energy (bottom axis) and incident photon energy (top axis). Different colors represent the separation of the energy ranges of vacuum ultraviolet (VUV) and soft x-ray light.[36] (b) The moment cuts along the k_z direction with photon energies of 7 eV and 21.2 eV. In order to indicate the k_z positions with different photon energies, we mark them in the same BZ. (c), (d) Photoemission intensity distributions of $CeTe_3$ along Γ–M near the Γ point with (c) 7 eV photons and (d) 21.2 eV photons. (e) Angle-integrated EDCs of $CeTe_3$ with 7 eV and 21.2 eV photons over the momentum range of $[-0.04\ \text{Å}^{-1}, 0.04\ \text{Å}^{-1}]$.

To compare the band structures of the surface and the bulk, we conducted ARPES measurements with 7 eV and 21.2 eV photons. Figure 6(a) displays the approximate inelastic mean free path of different photon energies, from which we find the measurements performed with 7 eV photons are more bulk sensitive than those taken with 21.2 eV photons. In the photoelectric process, the electron inelastic mean free path in solids with 21.2 eV is less than 1 nm or 2 monolayers, which makes the results more easily affected by the surface, while the inelastic mean free path of electrons with a laser is about 3–5 nm or 6–20 monolayers, so the detected photoemission signals are much more bulk sensitive. To exclude the effect of band structure discrepancy at different k_z positions, the moment cuts along the k_z direction with photon energies of 7 eV and 21.2 eV are shown in Fig. 6(b). To compare directly, we mark them in the same BZ, and find that the moment cuts taken with both energies locate at approximately $k_z = 17.6\%\ 2\pi/c$ along Γ–Z (M–A). Here we define $k_z = 0$ for the Γ points. Photoemission intensity distributions along Γ–M display apparent discrepancies in Figs. 6(c) and 6(d). Three major bands can be observed in the 7 eV spectrum, which are located at binding energies of 0.24 eV, 0.44 eV and 0.66 eV. These three bands can also be observed in the EDCs in Fig. 6(e). With 21.2 eV photons in Fig. 6(d), the band structure is quite different. Only two bands can be observed: one is narrow and locates at the lower binding energy, while the other is fairly broad and may consist of two peaks. The peak at 0.24 eV below E_F is almost at the same location with different photon energies as shown in Fig. 6(e), and the broad peak with 21.2 eV photons is at a similar position with the two peaks at 0.44 eV and 0.66 eV below E_F with 7 eV photons. To illustrate the intensity difference of the three bands in Figs. 6(c)–6(e), we can refer to the photoelectric cross section as a function of photon energy in Fig. 6(b).[37] With regard to the Te 5p orbital, the photoelectric cross section increases with decreasing photon energy in the range of low photon energy. This tendency is consistent with our experiment results and gives a reliable reason for the intensity differences of the two peaks at the binding energies of 0.24 eV and 0.66 eV. As for the peak at 0.44 eV below E_F, a reasonable deduction is that the hybridization between the 0.44 eV peak with other states may influence the intensity.

For $CeTe_3$, a prototypical CDW material, our research focuses on its f-electron features and additional influencing

factors such as temperature, light source energies and photon polarization. We observe that the f electrons present a dispersive quasiparticle band, indicating hybridization between the f electrons and conduction electrons. At the same time, the f electrons go through a localized to itinerant transition with changing temperature, which is common in other HF materials.[38–40] Besides, we find an energy gap in one conduction band, and the strong temperature-dependent behavior indicates that it may be related to the CDW transition. LV- and LH-polarized ARPES measurements reveal anisotropy of the orbitals with the same band, which shows different changes of intensity around the Γ and M points, and diverse orbital symmetries with different bands displaying various changing trends. With different energies, surface and bulk band structures are fairly similar in the locations of peaks, indicating the three bands observed in the valence band structure in Figs. 6(c)–6(e) are from the bulk state, which is common in some Ce-based materials.[41–43]

4. Conclusion

In summary, we have performed XRD, physical property and high-resolution ARPES measurements of the CDW f-electron compound $CeTe_3$. Our results illustrate the comprehensive electronic structure and f-electrons features in this CDW material. We find a weakly dispersive quasiparticle band around E_F which reflects the hybridization between f electrons and conduction electrons. Additionally, the localized to itinerant transition of f electrons and the energy gap probably induced by CDW are observed. We also discuss the influence of different photon energies and polarized photons on the band structure. Our findings illustrate the f-electrons properties in the CDW state of $CeTe_3$, revealing differences between the traditional HF materials and the CDW one, and contributing to the understanding of the microscopic properties of $CeTe_3$ and other rare-earth tellurides.

Acknowledgments

Project supported by the National Natural Science Foundation of China (Grant Nos. 12122409, 11874330, 11904334, 12004349, and 11904335), the National Key Research and Development Program of China (Grants Nos. 2022YFA1402201 and 2021YFA1601100), and the BL03U and BL09U ARPES beam line of Shanghai Synchrotron Radiation Facility (SSRF, China).

References

[1] Stewart G R 1984 *Rev. Mod. Phys.* **56** 755
[2] Pfleiderer C 2009 *Rev. Mod. Phys.* **81** 1551
[3] Yang Y F and Pines D 2008 *Phys. Rev. Lett.* **100** 096404
[4] Stockert O, Arndt J, Faulhaber E, Geibel C, Jeevan H S, Kirchner S, Loewenhaupt M, Schmalzl K, Schmidt W, Si Q and Steglich F 2011 *Nat. Phys.* **7** 119
[5] Shim J H, Haule K and Kotliar G 2007 *Science* **318** 1615
[6] Sato N K, Aso N, Miyake K, Shiina R, Thalmeier P, Varelogiannis G, Geibel C, Steglich F, Fulde P and Komatsubara T 2001 *Nature* **410** 340
[7] Zhang Y, Feng W, Lou X, Yu T L, Zhu X G, Tan S Y, Yuan B K, Liu Y, Lu H Y, Xie D H, Liu Q, Zhang W, Luo X B, Huang Y B, Luo L Z, Zhang Z J, Lai X C and Chen Q Y 2018 *Phys. Rev. B* **97** 045128
[8] Varma C M 1976 *Rev. Mod. Phys.* **48** 219
[9] Doniach S 1977 *Physica B+C* **91** 231
[10] Brouet V, Yang W L, Zhou X J, Hussain Z, Ru N, Shin K Y, Fisher I R and Shen Z X 2004 *Phys. Rev. Lett.* **93** 126405
[11] Shin K Y, Brouet V, Ru N, Shen Z X and Fisher I R 2005 *Phys. Rev. B* **72** 085132
[12] Hamlin J J, Zocco D A, Sayles T A, Maple M B, Chu J H and Fisher I R 2009 *Phys. Rev. Lett.* **102** 177002
[13] Zocco D A, Hamlin J J, Grube K, Chu J H, Kuo H H, Fisher I R and Maple M B 2015 *Phys. Rev. B* **91** 205114
[14] Iyeiri Y, Okumura T, Michioka C and Suzuki K 2003 *Phys. Rev. B* **67** 144417
[15] Tomic A, Rak Zs, Veazey J P, Malliakas C D, Mahanit S D, Kanatzidis M G and Tessmer S H 2009 *Phys. Rev. B* **79** 085422
[16] Malliakas C D and Kanatzidis M G 2006 *J. Am. Chem. Soc.* **128** 12612
[17] Ru N and Fisher I R 2006 *Phys. Rev. B* **73** 033101
[18] Chudo H, Michioka C, Itoh Y and Yoshimura K 2007 *J. Magn. Magn. Mater.* **310** 1105
[19] Chudo H, Michioka C, Itoh Y and Yoshimura K 2007 *Phys. Rev. B* **75** 045113
[20] Gweon G H, Denlinger J D, Clack J A, Allen J W, Olson C G, DiMasi E, Aronson M C, Foran B and Lee S 1998 *Phys. Rev. Lett.* **81** 886
[21] Ralević U, Lazarević N, Baum A, Eiter H M, Hackl R, Giraldo-Gallo P, Fisher I R, Petrovic C, Gajić R, Popović Z V 2016 *Phys. Rev. B* **94** 165132
[22] Komoda H, Sato T, Souma S, Takahashi T, Ito Y and Suzuki K 2004 *Phys. Rev. B* **70** 195101
[23] Leuenberger D, Sobota J A, Yang S L, Kemper A F, Giraldo-Gallo P, Moore R G, Fisher I R, Kirchmann P S, Devereaux T P and Shen Z X 2015 *Phys. Rev. B* **91** 201106
[24] DiMasi E, Foran B, Aronson M C and Lee S 1994 *Chem. Mater.* **6** 1867
[25] Deguchi K, Okada T, Chen G F, Ban S, Aso N and Sato N K 2009 *J. Phys.: Conf. Ser.* **150** 042023
[26] Chen D, Zhang S, Yang H X, Li J Q and Chen G F 2017 *J. Phys.: Condens. Matter* **29** 265803
[27] Brouet V, Yang W L, Zhou X J, Hussain Z, Moore R G, He R, Lu D H, Shen Z X, Laverock J, Dugdale S B, Ru N and Fisher I R 2008 *Phys. Rev. B* **77** 235104
[28] Chen Q Y, Xu D F, Niu X H, Jiang J, Peng R, Xu H C, Wen C H P, Ding Z F, Huang K, Shu L, Zhang Y J, Lee H, Strocov V N, Shi M, Bisti F, Schmitt T, Huang Y B, Dudin P, Lai X C, Kirchner S, Yuan H Q, and Feng D L 2017 *Phys. Rev. B* **96** 045107
[29] Chen Q Y, Wen C H P, Yao Q, Huang K, Ding Z F, Shu L, Niu X H, Zhang Y, Lai X C, Huang Y B, Zhang G B, Kirchner S and Feng D L 2018 *Phys. Rev. B* **97** 075149
[30] Chen Q Y, Xu D F, Niu X H, Peng R, Xu H C, Wen C H P, Liu X, Shu L, Tan S Y, Lai X C, Zhang Y J, Lee H, Strocov V N, Bisti F, Dudin P, Zhu J X, Yuan H Q, Kirchner S and Feng D L 2018 *Phys. Rev. Lett.* **120** 066403
[31] Fujimori S I, Fujimori A, Shimada K, Narimura T, Kobayashi K, Namatame H, Taniguchi M, Harima H, Shishido H, Ikeda S, Aoki D, Tokiwa Y, Haga Y and Ōnuki Y 2006 *Phys. Rev. B* **73** 224517
[32] Kim H D, Tjernberg O, Chiaia G, Kumigashira H, Takahashi T, Duò L, Sakai O, Kasaya M and Lindau I 1997 *Phys. Rev. B* **56** 1620
[33] Im H J, Ito T, Kim H D, Kimura S, Lee K E, Hong J B, Kwon Y S, Yasui A and Yamagami H 2008 *Phys. Rev. Lett.* **100** 176402
[34] Zhang K N, Liu X Y, Zhang H X, Deng K, Yan M Z, Yao W, Zheng M T, Schwier E F, Shimada K, Denlinger J D, Wu Y, Duan W H and Zhou S Y 2018 *Phys. Rev. Lett.* **121** 206402
[35] Wang Y, Ren J H, Li J H, Wang Y J, Peng H N, Yu P, Duan W H and Zhou S Y 2019 *Phys. Rev. B* **100** 241404
[36] Lv B Q, Qian T and Ding H 2019 *Nat. Rev. Phys.* **1** 609
[37] Yeh J J and Lindau I 1985 *At. Data Nucl. Data Tables* **32** 1
[38] Fujimori S I, Saitoh Y, Okane T, Fujimori A, Yamagami H, Haga Y, Yamamoto E and Ōnuki Y 2007 *Nat. Phys.* **3** 618

[39] Bittar E M, Adriano C, Giles C, Rettori C, Fisk Z and Pagliuso P G 2012 *Phys. Rev. B* **86** 125108

[40] Koizumi A, Motoyama G, Kubo Y, Tanaka T, Itou M and Sakurai Y 2011 *Phys. Rev. Lett.* **106** 136401

[41] Mende M, Ali K, Poelchen G, Schulz S, Mandic V, Tarasov A V, Polley C, Generalov A, Fedorov A V, Güttler M, Laubschat C, Kliemt K, Koroteev Y M, Chulkov E V, Kummer K, Krellner C, Usachov D Y and Vyalikh D V 2022 *Adv. Electron. Mater.* **8** 2100768

[42] Patil S, Generalov A, Güttler M, Kushwaha P, Chikina A, Kummer K, Rödel T C, Santander-Syro A F, Caroca-Canales N, Geibel C, Danzenbächer S, Kucherenko Y, Laubschat C, Allen J W and Vyalikh D V 2016 *Nat. Commun.* **7** 11029

[43] Poelchen G, Schulz S, Mende M, Güttler M, Generalov A, Fedorov A V, Caroca-Canales N, Geibel C, Kliemt K, Krellner C, Danzenbächer S, Usachov D Y, Dudin P, Antonov V, Allen J, Laubschat C, Kummer K, Kucherenko Y and Vyalikh D 2020 *npj Quantum Mater.* **5** 70